Localizing Dynamically Formed Black Hole Binaries in Milky Way Globular Clusters with LISA

Zeyuan Xuan[1,2] , Kyle Kremer[3] , and Smadar Naoz[1,2]

[1] Department of Physics and Astronomy, UCLA, Los Angeles, CA 90095, USA; zeyuan.xuan@physics.ucla.edu
[2] Mani L. Bhaumik Institute for Theoretical Physics, Department of Physics and Astronomy, UCLA, Los Angeles, CA 90095, USA
[3] Department of Astronomy and Astrophysics, University of California, San Diego, 9500 Gilman Drive, La Jolla, CA 92093, USA

Abstract

The dynamical formation of binary black holes (BBHs) in globular clusters (GCs) may contribute significantly to the observed gravitational-wave (GW) merger rate. Furthermore, the Laser Interferometer Space Antenna (LISA) may detect many BBH sources from GCs at mHz frequencies, enabling the characterization of such systems within the Milky Way and nearby Universe. In this work, we use Monte Carlo N-body simulations to construct a realistic sample of Galactic clusters, thus estimating the population, detectability, and parameter measurement accuracy of BBHs hosted within them. In particular, we show that the GW signal from 0.7 ± 0.7, 2.0 ± 1.7, 3.6 ± 2.3, and 13.4 ± 4.7 BBHs in Milky Way GCs can exceed the signal-to-noise ratio (SNR) threshold of SNR = 30, 5, 3, and 1 for a 10 yr LISA observation, with $\sim 50\%$ of detectable sources exhibiting high eccentricities ($e \gtrsim 0.9$). Moreover, the Fisher matrix and Bayesian analyses of the GW signals indicate that these systems typically feature highly resolved orbital frequencies ($\delta f_{\rm orb}/f_{\rm orb} \sim 10^{-7}$ to 10^{-5}) and eccentricities ($\delta e/e \sim 10^{-3}$ to 0.1), as well as a measurable total mass when SNR exceeds ~ 20. Notably, we show that high-SNR BBHs can be confidently localized to specific Milky Way GCs with a sky localization accuracy of $\delta\Omega \sim 1 \deg^2$, and we address the large uncertainties in their distance measurement ($\delta R \sim 0.3$–$20 \,{\rm kpc}$). The detection and localization of even a single BBH in a Galactic GC would allow accurate tracking of its long-term orbital evolution, enable a direct test of the role of GCs in BBH formation, and provide a unique probe into the evolutionary history of Galactic clusters.

Unified Astronomy Thesaurus concepts: Gravitational waves (678); Gravitational wave sources (677)

1. Introduction

The LIGO/Virgo/KAGRA (LVK) collaboration (e.g., The LIGO Scientific Collaboration et al. 2023) has detected approximately 100 extragalactic binary black hole (BBH) mergers (e.g., R. Abbott et al. 2023). However, the formation channels for these mergers remain unclear, with various proposed mechanisms potentially contributing, including isolated binary evolution (e.g., K. Belczynski et al. 2016; S. Stevenson et al. 2017; J. J. Eldridge et al. 2019), dynamical formation in galactic centers (B. Kocsis & J. Levin 2012a; B.-M. Hoang et al. 2019; A. P. Stephan et al. 2019; M. Arca Sedda et al. 2023; Z. Zhang & X. Chen 2024), galactic fields (E. Michaely & H. B. Perets 2019, 2020; E. Michaely & S. Naoz 2022; J. Stegmann et al. 2024), globular clusters (GCs; e.g., C. L. Rodriguez et al. 2016b; G. Fragione & O. Bromberg 2019; K. Kremer et al. 2020), active galactic nucleus disks (P. Peng & X. Chen 2021; H. Tagawa et al. 2021; D. J. Muñoz et al. 2022; J. Samsing et al. 2022; H. Gautham Bhaskar et al. 2023), hierarchical triple systems (L. Wen 2003; S. Naoz 2016; B.-M. Hoang et al. 2018; F. Antonini & M. Gieles 2020a), and primordial BH scenarios (S. Bird et al. 2016; M. Sasaki et al. 2016). A key challenge in distinguishing these channels arises from the large distances and limited sky localization accuracy of extragalactic BBH mergers (e.g., S. Vitale & C. Whittle 2018), which prevent confident identification of specific host environments. On the other hand, the future Laser Interferometer Space Antenna (LISA;

P. Amaro-Seoane et al. 2017) will observe BBHs in a lower frequency band (10^{-4} to 10^{-1} Hz), which potentially allows us to probe their earlier evolutionary stages in the local Universe and distinguish between different hosting environments (see, e.g., L. Barack & C. Cutler 2004; B. Mikóczi et al. 2012; T. Robson et al. 2018; X. Chen et al. 2019; Y. Fang et al. 2019; B.-M. Hoang et al. 2019; K. Breivik et al. 2020; N. Tamanini et al. 2020; A. Torres-Orjuela et al. 2021; H. Wang et al. 2021; Z. Xuan et al. 2021; F. Zhang et al. 2021; P. Amaro-Seoane et al. 2023; S. Naoz et al. 2022; S. Naoz & Z. Haiman 2023).

In particular, GCs are considered ideal places for the dynamical formation of mHz BBHs (M. J. Benacquista et al. 2001; M. C. Miller & D. P. Hamilton 2002; S. F. Portegies Zwart & S. L. W. McMillan 2002; M. Morscher et al. 2015; C. L. Rodriguez et al. 2015, 2016a; D. J. D'Orazio & J. Samsing 2018; J. Samsing 2018; D. Gerosa et al. 2019; K. Kremer et al. 2019a; J. Samsing & D. J. D'Orazio 2019; M. Zevin et al. 2019; S. Vitale 2021). For example, a large number of BHs can form through stellar evolution in clusters (see, e.g., P. Kroupa 2001; M. Morscher et al. 2015). Due to mass segregation, these BHs gradually sink to the cluster core on sub-Gyr timescales, leading to the formation of a BH-dominated central region (L. Spitzer 1969; S. R. Kulkarni et al. 1993; S. Sigurdsson & L. Hernquist 1993). In the BH-dominated core, dynamically hard BH binaries promptly form through three-body interactions and further harden through gravitational-wave (GW) capture, binary−single, and binary−binary scattering events (D. C. Heggie 2001; D. Merritt et al. 2004; A. D. Mackey et al. 2007; P. G. Breen & D. C. Heggie 2013; M. Peuten et al. 2016; L. Wang et al. 2016; M. Arca Sedda et al. 2018; K. Kremer et al. 2018a, 2020; M. Zevin et al. 2019; A. Zocchi et al. 2019;

F. Antonini & M. Gieles 2020b). Collectively, these dynamical processes result in BBH merger events at an estimated rate of $\mathcal{R}_0 \approx 7.2^{+21.5}_{-5.5} \mathrm{Gpc}^{-3}\mathrm{yr}^{-1}$ in the local Universe (e.g., C. L. Rodriguez et al. 2016b; F. Antonini & M. Gieles 2020b; K. Kremer et al. 2020), potentially making a significant contribution to the total GW merger rate detected by the LVK.

Moreover, dynamically formed BBHs in GCs can provide valuable information about their astrophysical environment. For example, BBH mergers in a dense stellar environment typically have nonnegligible eccentricity (e.g., R. M. O'Leary et al. 2009; T. A. Thompson 2011; S. J. Aarseth 2012; B. Kocsis & J. Levin 2012a; K. Breivik et al. 2016; D. J. D'Orazio & J. Samsing 2018; J. Samsing et al. 2019; M. Zevin et al. 2019; F. Antonini & M. Gieles 2020b; K. Kremer et al. 2020; M. A. S. Martinez et al. 2020; M. Winter-Granić et al. 2024; B. Rom et al. 2024), which could greatly enhance our understanding of their formation mechanisms (see, e.g., W. E. East et al. 2013; J. Samsing et al. 2014; M. Coughlin et al. 2015; K. Breivik et al. 2016; S. Vitale 2016; A. Nishizawa et al. 2017; M. Zevin et al. 2017, 2021b; L. Gondán et al. 2018b, 2018a; M. E. Lower et al. 2018; C. J. Moore et al. 2019; I. M. Romero-Shaw et al. 2019; R. Abbott et al. 2021; The LIGO Scientific Collaboration et al. 2023), improve parameter estimation accuracy (Z. Xuan et al. 2023), or help with detecting the presence of tertiary companions through eccentricity oscillations (T. A. Thompson 2011; J. M. Antognini et al. 2014; B.-M. Hoang et al. 2018, 2020; A. P. Stephan et al. 2019; M. A. S. Martinez et al. 2020; S. Naoz et al. 2020; H. Wang et al. 2021; A. M. Knee et al. 2022). Further, as shown by recent studies, many BBHs undergo a wide (semimajor axis $a \gtrsim 0.1$ au), highly eccentric (eccentricity $e \gtrsim 0.9$) progenitor stage before the final merger (see, e.g., B. Kocsis & J. Levin 2012a; B.-M. Hoang et al. 2019; Z. Xuan et al. 2024b; A. M. Knee et al. 2024), which can also have unique imprints on mHz GW detections (Z. Xuan et al. 2024a, 2025).

In this work, we will explore the properties of dynamically formed BBHs in Milky Way GCs, with a focus on their detectability and parameter measurement accuracy in the mHz GW detection of LISA. Particularly, previous studies have shown that LISA can detect a handful of BBHs formed through isolated binary channels in the Milky Way (see, e.g., A. Lamberts et al. 2018; A. Sesana et al. 2020; T. Wagg et al. 2022; P. Tang et al. 2024). On the other hand, with approximately 150 GCs in the Milky Way (e.g., W. E. Harris 1996; H. Baumgardt & M. Hilker 2018), we expect a significant number of dynamically formed BBH sources from these clusters (see, e.g., K. Kremer et al. 2018a), for which more specific predictions of their population are still needed.

We highlight that the detection of even a single BH in Milky Way GCs would provide a direct test of the role of GCs in BBH formation, offering valuable insights into the relative contributions of different formation channels to the observed BBH population. Therefore, it is essential to create a realistic sample of GCs that harbor BBHs in the Milky Way, which will enable us to constrain the underlying populations of BHs and BBHs in GCs and assess which specific Galactic GCs are most likely to host resolvable BBHs within the LISA frequency band.

This Letter is organized as follows: In Section 2, we introduce the simulation of GCs (the CMC Cluster Catalog cluster model) used in this work. Next, we fit the simulated clusters to Galactic GCs, thus estimating the population of Galactic BBHs in GCs today. Based on the simulations, we estimate the number of BBHs detectable by LISA, their eccentricity and mass distributions (see Section 3.1), and which specific Galactic GCs are most likely to host these sources (see Section 3.2). Furthermore, we adopt the Fisher matrix and Bayesian analyses in Section 3.3 and assess the parameter measurement accuracy of BBHs in the Milky Way GCs. In Section 4, we summarize the results and discuss the astrophysical implications. Throughout the Letter, unless otherwise specified, we set $G = c = 1$.

2. Creating a Mock Galactic Sample

To assemble a realistic sample of GC BBHs, we use the CMC Cluster Catalog cluster models of K. Kremer et al. (2020). This suite of models is computed using the Monte Carlo N-body dynamics code CMC, which includes the most up-to-date physics for studying the formation and evolution of BHs in dense clusters (for a review, see C. L. Rodriguez et al. 2022). Each of the 148 independent simulations of this catalog models the gravitational dynamics and stellar evolution for each of the N stars in the system, keeping track of various properties (e.g., masses, semimajor axis, eccentricity) of all BBHs present in the cluster from formation to present day. The CMC Cluster Catalog has been tested rigorously against observations of Galactic GCs and successfully reproduces global features like surface brightness profiles, velocity dispersion profiles, and color–magnitude diagrams (N. Z. Rui et al. 2021), as well as specific compact object populations including millisecond pulsars (C. S. Ye et al. 2019), X-ray binaries (K. Kremer et al. 2019a), cataclysmic variables (K. Kremer et al. 2021), and connections to BBHs observed by LIGO/Virgo (K. Kremer et al. 2020).

For this study, we aim to predict which specific Galactic GCs are most likely to host resolvable LISA sources at present. In this case, we must identify a single "best-fit" model from the CMC Cluster Catalog for each observed Milky Way GC. The CMC Catalog models can be sorted into a three-dimensional grid in $M_{\mathrm{cl}} - Z - R_{\mathrm{gc}}$ space, where M_{cl} is the total cluster mass at present (set by our choice of initial $N = [2, 4, 8, 16, 32] \times 10^5$ stars and evolved to the current value), $Z = [0.01, 0.1, 1] \times Z_\odot$ is the current cluster metallicity, and $R_{\mathrm{gc}} = [2, 8, 20]$ kpc is the current Galactocentric position. For a given observed GC, we identify the appropriate $M_{\mathrm{cl}} - Z - R_{\mathrm{gc}}$ model bin based on that GC's observed mass and metallicity values (taken from W. E. Harris 2010). Each distinct $M_{\mathrm{cl}} - Z - R_{\mathrm{gc}}$ bin contains four models of varying initial virial radius, which determines the clusters' final core and half-light radius. To find the single best-fit model, we identify the model in the appropriate $M_{\mathrm{cl}} - Z - R_{\mathrm{gc}}$ bin that has core radius at $t = 12$ Gyr closest to the observed core radius value (W. E. Harris 2010).[4] Once the best-fit model is identified, we select a cluster age by randomly sampling from that model's available time snapshot outputs in the range 8–13.7 Gyr (typically this consists of a sample of 10–50 snapshots per model). This range is intended to reflect the uncertainty in cluster ages at present. Once a cluster snapshot is selected, we then identify the number and properties of all BBHs present in the best-fit model at that time. By repeating these steps for each observed GC, we build a sample of the full population of BBHs present in each of the Milky Way's GCs at present. We then repeat this full procedure 10 times to

---

[4] We also tried fitting using half-light radius in place of core radius and found no major differences in our results.
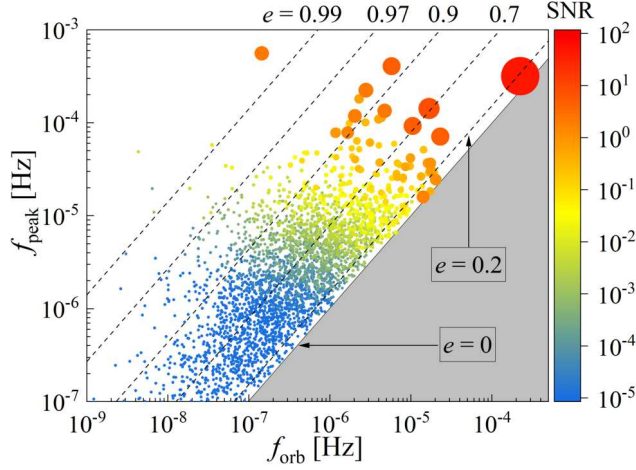
Figure 1. An example of a simulated BBH population in Milky Way GCs. Here we plot the orbital frequency and peak GW frequency of BBH systems from a single realization of our simulated Milky Way GCs (see Equation (1)). The SNR of each BBH, estimated analytically using Equation (2) for a 5 yr LISA observation, is represented by different colors. Detectable BBHs, based on their SNR, are highlighted with enlarged circles. Dashed lines indicate the eccentricity of BBHs in different regions, with $e = 0.99, 0.97, 0.9, 0.7, 0.2, 0$, from left to right. The simulated BBHs have an average component mass of $m_1 = 15.56\,M_\odot$, $m_2 = 15.21\,M_\odot$ for in-cluster BBHs and $m_1 = 20.73\,M_\odot$, $m_2 = 20.46\,M_\odot$ for ejected BBHs, but the mass of individual systems may vary.

assemble 10 separate Galactic realizations (the random time snapshot draw enables us to create 10 distinct samples).

Once this population is assembled, we compute the GW strain for each of the individual BBHs predicted within each Galactic cluster at present. Component masses, semimajor axes, and eccentricities are obtained directly from our best-fit CMC snapshot, and the source distance is simply the heliocentric distance of the GC of interest (W. E. Harris 2010).

Figure 1 shows an example of the simulated BBH population in Milky Way GCs. In particular, we choose one representative Galactic realization from the best-fit result of the CMC Catalog and plot the orbital frequency (f_{orb}) and the peak GW frequency (f_{peak}) of each BBH system (e.g., R. M. O'Leary et al. 2009):

$$f_{peak} = f_{orb}(1 + e)^{1/2}(1 - e)^{-3/2}. \quad (1)$$

We note that most of the dynamically formed systems have nonnegligible eccentricity. In this case, f_{peak} of the eccentric GW signal indicates the frequency of the peak GW power, which typically needs to be within the mHz band for LISA to detect the source. Furthermore, in Figure 1 we can estimate the eccentricity of each system by comparing f_{peak} and f_{orb} (see the dashed lines with $e = 0.99, 0.97, 0.9, 0.7, 0.2, 0$, from left to right). For example, a system with $f_{peak} \sim f_{orb}$ should have moderate eccentricity, and a system with $f_{peak} \gg f_{orb}$ is highly eccentric.

In Figure 1, we use different colors to represent the signal-to-noise ratio (SNR) of BBHs, which is estimated analytically by summing the contributions from all the harmonics of their GW signal (see, e.g., P. C. Peters & J. Mathews 1963; B. Kocsis & J. Levin 2012a; Z. Xuan et al. 2024b):

$$\text{SNR}^2 = 8h_0^2(a)\sum_n \frac{g(n, e)}{S_n(nf_{orb})n^2}T_{obs}, \quad (2)$$

in which $n = 1, 2, 3 \ldots$ represents the number of harmonics, T_{obs} is the observation time, and $h_0(a) = \sqrt{32/5}\,m_1m_2/(Ra)$

depends on the binary's component mass m_1, m_2, semimajor axis a, and distance R. Additionally, $S_n(f)$ is the spectral noise density of LISA evaluated at GW frequency f (we adopt the LISA-N2A5 noise model; see, e.g., A. Klein et al. 2016; T. Robson et al. 2019), and $g(n, e)$ can be evaluated using

$$
\begin{aligned}
g(n, e) &= \frac{n^4}{32}\Bigg[\left(J_{n-2} - 2eJ_{n-1} + \frac{2}{n}J_n + 2eJ_{n+1} - J_{n+2}\right)^2 \\
&+ (1 - e^2)(J_{n-2} - 2J_n + J_{n+2})^2 + \frac{4}{3n^2}J_n^2\Bigg], \quad (3)
\end{aligned}
$$

in which J_i is the ith Bessel function evaluated at ne.

We note that the estimation of SNR in Equation (2) is based on the sky-average power of GW emission. In reality, the inclination and sky location of the GW source will also affect the detected SNR, making it different from the average value. Therefore, the value of SNR shown in Figure 1 should be understood as a heuristic estimation (in most cases, the variation in SNR caused by different inclinations is within an order of magnitude of the average value). For a detailed discussion, see the Appendix of Z. Xuan et al. (2024b).

As can be seen in Figure 1, the simulated orbital frequency and eccentricity of BBHs in Milky Way GCs distribute in a wide range of parameter space, with the majority of the binaries lying below the threshold of SNR = 5 for a 5 yr LISA observation. However, there can be a handful of detectable sources with both moderate and high eccentricities. For example, we identified three detectable sources in this realization, which have the orbital parameters of $f_{orb} = 2.24 \times 10^{-4}$ Hz, 1.67×10^{-5} Hz, 5.79×10^{-6} Hz ($a = 0.0075, 0.048, 0.079$ au) and $e = 0.17, 0.71, 0.93$, respectively. Furthermore, there is a larger number ($\sim$20) of highly eccentric BBHs in the region of SNR $\sim$ 1–5 (see the orange and yellow circles), which could be detected by LISA given a longer observation time, or contribute to a stochastic background of GW bursts (see, e.g., Z. Xuan et al. 2024a).

3. Source Localization and Astrophysical Implications

3.1. Detectability and Eccentricity Distribution

Based on the simulation in Section 2, we computed the expected number of detectable BBHs formed in Milky Way GCs. In total, we expect the GW signal from 0.7 ± 0.7, 2.0 ± 1.7, 3.6 ± 2.3, and 13.4 ± 4.7 BBHs to exceed the threshold of SNR = 30, 5, 3, and 1, respectively, for a 10 yr observation of LISA.[5] Furthermore, the simulation yields significant eccentricity for all the detectable BBH systems, with eccentricity ranges from 0.167 to 0.994 for systems with SNR > 3, which is consistent with the expected eccentricity distribution of dynamically formed binaries in GCs (see, e.g., K. Kremer et al. 2018a, for LISA source expectations from Newtonian modeling of GCs).

We highlight that $\sim$50% of the BBHs with SNR > 5 have high eccentricity in the detection ($e \gtrsim 0.9$); the fraction becomes even larger ($\sim$70%) for the population with SNR $\sim$ 1–5. This phenomenon reflects the highly eccentric nature of compact binary formation in a dense stellar environment. It also indicates that most of the GW signals

---

[5] Here the error bar reflects the standard derivative of BBH number in each SNR bin, accounting for 10 realizations in the simulation (see Section 2).

from BBHs in Galactic GCs will be characterized by "repeated bursts" (Z. Xuan et al. 2024b), for which the detectability and parameter extraction accuracy have been recently investigated (Z. Xuan et al. 2025).

The large fraction of highly eccentric BBHs can be understood analytically. In particular, the GW signal from eccentric binaries is made up of multiple harmonics, some of which have frequencies much higher than the binary's orbital frequency (see, e.g., Equation (1)). Therefore, compared with circular BBHs, eccentric sources in GCs could enter the sensitive band of LISA with a much wider orbital separation a, when their f_{orb} is well below the mHz band. In other words, these eccentric binaries will be detected at the earlier evolution stages, with more extended lifetimes and larger number expectations than circular sources in the same frequency band. For example, highly eccentric, stellar-mass BBHs can stay in the mHz GW band with a lifetime of (P. C. Peters & J. Mathews 1963; Z. Xuan et al. 2024a)

$$\tau_{ecc} \sim \frac{3}{85\mu M^2} a^4 (1 - e^2)^{7/2}$$
$$\sim 1.17 \times 10^6 \, yr \, \frac{2}{q(1 + q)} \left(\frac{M}{20 \, M_\odot}\right)^{-3}$$
$$\times \left(\frac{a}{1 \, au}\right)^4 \left(\frac{1-e}{0.002}\right)^{\frac{7}{2}}, \quad (4)$$

where $M = m_1 + m_2$, $\mu = m_1 m_2/(m_1 + m_2)$, and $q = m_1/m_2$. Note that this timescale is much longer than the merger timescale of a circular BBH system in the mHz band (which typically lasts for $\sim 10^3$–10^5 yr). Thus, these highly eccentric BBHs may dominate the population of BBHs in the local Universe, where their GW signals are strong enough to be identified.[6]

Additionally, binary mergers originating from GCs can be categorized into different types, based on their evolution history. On top of the binaries merging within the GC after dynamical interactions (in-cluster mergers), a significant fraction of BBHs can undergo multiple hardening encounters before being ejected from the cluster, eventually merging in the galactic field (ejected mergers; see, e.g., J. M. B. Downing et al. 2010; C. L. Rodriguez et al. 2016a, 2018; K. Kremer et al. 2019b). In our simulations, we find that in-cluster BBHs contribute approximately 0.7, 1.5, 2.2, and 5.8 GW sources, while the ejected population contributes around 0, 0.5, 1.4, and 7.6 GW sources above the thresholds of SNR = 30, 5, 3, and 1, respectively, for a 10 yr LISA observation.

3.2. The Location of Gravitational-wave Sources

Next, we analyze which specific Galactic GCs are most likely to host resolvable BBHs, using the CMC Catalog from K. Kremer et al. (2020). In particular, we take the observational properties of Milky Way GCs following W. E. Harris (2010) (see circles in Figure 2) and choose the best-fit model in the CMC Catalog that matches the mass, metallicity, Galactic position, and core radius of each cluster (see Section 2). For each fitted

cluster, we then compute the population properties of BHs and estimate their expectation of hosting a detectable BBH system.

The results are summarized in Figure 2. Specifically, the left panel depicts the ratio of the clusters' core radius to the half-light radius, r_c/r_h (y-axis), versus their distance, R, from the detector (x-axis); the right panel shows the estimated total mass of each cluster, M_{GC}, against their distance R (x-axis) (see W. E. Harris 2010). In Figure 2, the size of filled circles represents the expected probability for a cluster to host a BBH system with SNR > 1:

$$P(SNR > 1) = \frac{N_{SNR>1}}{N_{realization}}, \quad (5)$$

where $N_{realization} = 10$ represents the total number of realizations for Milky Way GCs (see Section 2), and $N_{SNR>1}$ represents the total number of BBHs with SNR > 1 in a GC, summed across all the realizations.

The color of circles in Figure 2 represents the detectability of their largest SNR GW source in the simulation, with colors ranging from yellow to red. Furthermore, we use filled blue circles to represent GCs with no detectable BBHs (maximum SNR < 1) and open gray circles to represent GCs without any BBHs in the simulation at all. In the figure, we highlight the names of the eight fitted GCs that we predict are most likely to host detectable BBHs.

As illustrated in Figure 2, GCs with a high probability of hosting detectable BBHs tend to cluster within specific regions of the parameter space. Notably, we predict that detectable BBHs are most likely to be resolved in GCs that are close in distance ($R \lesssim 10$ kpc), exhibit a small r_c/r_h (~ 0.1–0.3, indicative of denser, more dynamically active GCs; see the left panel), and have a large total mass (see the right panel).

3.3. Astrophysical Implication

In this section, we first adopt the Fisher matrix analysis to explore the astrophysical information that can be extracted from dynamically formed BBHs in Milky Way GCs. This method is commonly used as a linearized estimation of the parameter measurement error in the high-SNR limit (see, e.g., C. Cutler & É. E. Flanagan 1994; D. Coe 2009). For completeness, we briefly summarize the relevant equations and waveform model used in this work (see our previous works, Z. Xuan et al. 2023, 2025, for similar applications).

We begin by defining the noise-weighted inner product between two gravitational waveforms, $h_1(t)$ and $h_2(t)$, as follows:

$$\langle h_1 | h_2 \rangle = 2 \int_0^\infty \frac{\tilde{h}_1(f)\tilde{h}_2^*(f) + \tilde{h}_1^*(f)\tilde{h}_2(f)}{S_n(f)} df, \quad (6)$$

where $\tilde{h}_l$ (with $l = 1, 2$) denotes the Fourier transform of the waveform and the asterisk represents the complex conjugate.

Representing the parameters of a GW source as a vector $\boldsymbol{\lambda}$, the GW waveform h can be expressed as $h(t; \boldsymbol{\lambda})$. The Fisher matrix is then defined as

$$F_{ij} = \left\langle \frac{\partial h(\boldsymbol{\lambda})}{\partial \lambda_i} \bigg| \frac{\partial h(\boldsymbol{\lambda})}{\partial \lambda_j} \right\rangle, \quad (7)$$

where λ_i denotes the ith parameter of the waveform.

Let C denote the inverse of the Fisher matrix, $C = F^{-1}$. This matrix approximates the sample covariance matrix of the Bayesian posterior distribution for the parameters of the GW

---

[6] However, stellar-mass BBHs at larger distances are unlikely to be detected with high eccentricity (e.g., at a few hundred Mpc, detectable BBHs in GCs have eccentricities of at most 0.01, as shown in K. Kremer et al. 2019b). This is because highly eccentric sources, in general, have a smaller power of GW emission, but LISA can only detect high-SNR GW sources at cosmological distances.
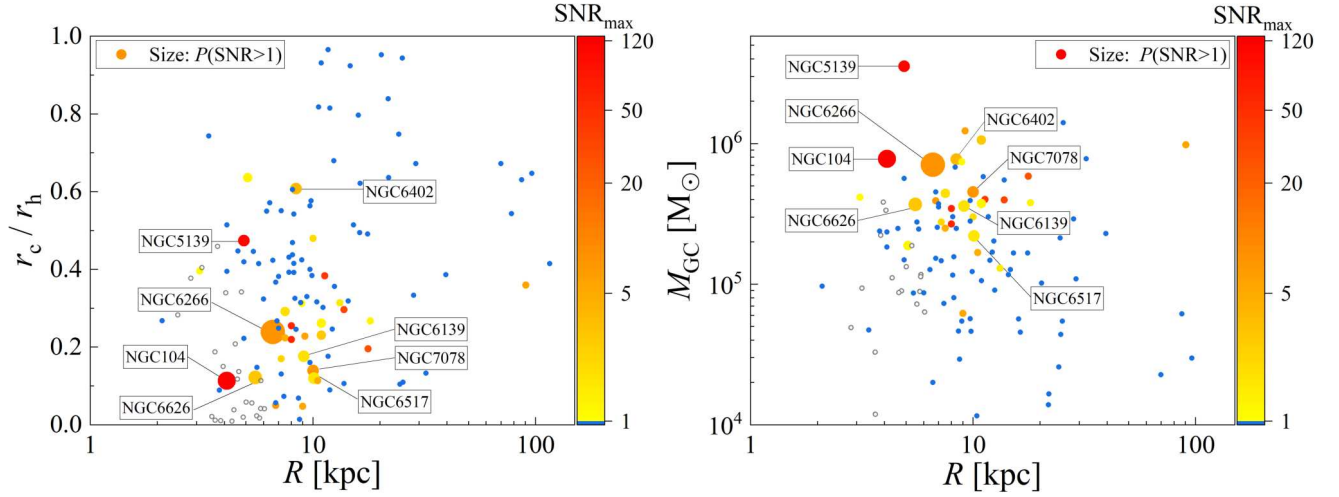
Figure 2. Properties of Milky Way GCs likely to host detectable BBHs in the mHz GW band. Here we adopt the simulation results of the BBH population in the Milky Way GCs, based on 10 realizations of in-cluster sources. The size of filled circles represents the expected probability for a cluster to host a BBH system with SNR > 1, $P(\text{SNR} > 1)$, and the color represents the maximum SNR of detectable BBHs, assuming a 10 yr observation. The left panel plots the distance R (x-axis) against the ratio of the core radius to the half-light radius, r_c/r_h (y-axis); the right panel plots the distance R (x-axis) against the estimated total mass M_{GC} of each GC. The largest circle corresponds to the GC hosting nine BBHs with SNR > 1 across the 10 realizations (i.e., an expected probability of ~90%), while the smallest circles represent GCs hosting one BBH system with SNR > 1 (expected probability ~10%). Filled blue circles represent GCs with no detectable BBHs (maximum SNR < 1), and open gray circles represent GCs without any BBHs in the simulation. We highlight the names of the top eight GCs most likely to host detectable BBHs.

source. Using this, we estimate the error in parameter measurement as follows:

$$\delta\lambda_i = \sqrt{\langle(\Delta\lambda_i)^2\rangle} = \sqrt{C_{ii}}. \qquad (8)$$

To evaluate Equations (6)–(8) numerically, we further compute the GW signal, $h(t)$, from eccentric BBHs. Specifically, we adopt the x-model (I. Hinder et al. 2010) for the waveform generation, assuming that the binaries undergo isolated evolution during observation. The x-model is a time-domain, post-Newtonian (pN)–based waveform family, designed to capture all key features introduced by eccentricity in nonspinning binaries (E. A. Huerta et al. 2014). It has been validated against numerical relativity for equal-mass BBHs with $e = 0.1$, covering 21 cycles before the merger, and also aligns with well-established waveform template families used in GW data analysis for the zero-eccentricity case (D. A. Brown & P. J. Zimmerman 2010). In this model, the binary orbit is described using the Keplerian parameterization at 3 pN order, with the conservative evolution also given to 3 pN order. The energy and angular momentum losses are mapped to changes in the orbital eccentricity e and the pN expansion parameter $x \equiv (\omega M)^{2/3}$, where ω is the mean Keplerian orbital frequency. These two parameters evolve according to 2 pN equations. We note that stellar-mass BBHs in the local Universe typically have a pericenter distance larger than ~10^{-3} au in the mHz GW band (including the highly eccentric BBHs; see, e.g., Z. Xuan et al. 2024b, 2024a). Thus, their gravitational field is much weaker than the strength of the field for which the x-model has been validated against numerical relativity, and the x-model represents a plausible description of their GW signal.[7]

Furthermore, we include the detector's annual motion around the Sun to analyze the realistic detection of Milky Way BBHs (the detector response function; see, e.g., C. Cutler 1998; N. J. Cornish & L. J. Rubbo 2003; B. Kocsis et al. 2007, for more details). Consequently, the GW signal from an eccentric binary can be parameterized using

$$h(t) = h(t; \boldsymbol{\lambda} = \{f_{\text{orb},0}, 1 \\ - e_0, M, q, \cos\Theta, \Phi, \cos\theta, \phi, R, \psi\}), \qquad (9)$$

in which $f_{\text{orb},0}$ and e_0 are the initial orbital frequency and eccentricity of the binary, respectively;[8] Θ and Φ represent the spherical polar angles of the observer as viewed in the nonrotating, comoving frame of the compact object binary (i.e., the propagation direction of the GW signal viewed in the source's frame); θ and ϕ are the spherical polar angles describing the sky location of the GW source viewed in the comoving frame of the solar system, where the LISA detector undergoes annual motion around the Sun; R is the binary's distance from the detector (which is set as the distance of the GC hosting this binary); and ψ is the polarization angle of the GW signal. For more details on the parameterization, see Section B in Z. Xuan et al. (2025).

After generating the GW signal as described by Equation (9), we compute the partial derivatives of the waveform with respect to each parameter (see Equation (7)). For example, to calculate $\partial h/\partial M$, we vary the total mass $M \to M' = M + \Delta M$ and generate a new waveform $h'(t) = h'(t; \boldsymbol{\lambda}')$, where $\boldsymbol{\lambda}' =$. The partial derivative is then approximated as $\partial h/\partial M \approx [h'(t) - h(t)]/\Delta M$. Note that each partial derivative is a time series representing the difference in the waveform caused by slightly varying one of the parameters around the central value. In

---

[7] In addition, there have been recent studies focusing on fast and accurate waveform generation, such as for the case of eccentric extreme mass ratio inspirals (A. J. K. Chua et al. 2021; S. A. Hughes et al. 2021; M. L. Katz et al. 2021). However, the mass (~$10\,M_\odot$) and eccentricity range (~0.1–0.999) of BBHs we discuss here are different. Therefore, we adopt the x-model for simplicity.

[8] Hereafter we use f_{orb} as an abbreviation for the initial orbital frequency $f_{\text{orb},0}$, which is related to the initial semimajor axis a_0 via $f_{\text{orb},0} = (2\pi)^{-1}M^{1/2}a_0^{-3/2}$, and we use e as an abbreviation for the initial eccentricity e_0.

addition, in the numerical computation, we choose the parameter variation $d\lambda_i$ such that $\langle dh | dh \rangle \sim 10^{-3} \langle h | h \rangle$, ensuring that the change in the waveform is small when computing the numerical derivative.

Finally, we compute the inner products between derivative waveforms using Equation (6) and then substitute the results into Equation (7) to calculate F_{ij}. The parameter measurement errors are then estimated by inverting F_{ij}, as described in Equation (8)). We summarize the results in Figures 3 and 4 (note that Fisher matrix analysis yields the measurement error for all the parameters, $\{f_{\mathrm{orb},0}, 1 - e_0, M, q, \cos\Theta, \Phi, \cos\theta, \phi, R, \psi\}$, but here we only show some of them to avoid clustering).

In Figure 3, we present a realistic example of the parameter measurement error for BBHs in Milky Way GCs. The white stars in the figure represent all the in-cluster and ejected BBHs from one realization of our simulated Milky Way GCs. In the background, we use different colors to show the parameter measurement errors, $\delta\lambda_i$, as a function of the BBHs' orbital parameters, $(a, 1 - e)$. Particularly, panel (a) shows the relative error in orbital frequency measurement, $\delta f_{\mathrm{orb}}/f_{\mathrm{orb}}$; panel (b) shows the relative error in eccentricity measurement, $\delta e/e$; panel (c) shows the relative error in total mass, $\delta M/M$; and panel (d) shows the absolute error in sky location ($2a_s$, as the major axis of the sky error ellipsoids; see, e.g., R. N. Lang & S. A. Hughes 2006; B. Kocsis et al. 2007, 2008; B. Mikóczi et al. 2012). To ensure consistency in mapping the parameter measurement errors, we fix specific BBH parameters when computing the Fisher matrix results shown in Figure 3 ($m_1 = 10\ M_\odot$, $m_2 = 15\ M_\odot$, $R = 8\,\mathrm{kpc}$, and $\Phi = \Theta = \theta = \phi = \pi/4$, assuming a 5 yr observation). However, BBHs in Milky Way GCs can have different mass, inclination, and sky locations, which potentially affects their parameter measurement.[9] Therefore, the value shown by background colors in Figure 3 should be interpreted as heuristic estimates of the realistic accuracy.

We highlight that the estimation shown in Figure 3 is agnostic to different BBH formation channels. In other words, for any potential BBH population in the galaxy, not necessarily from the GCs, their orbital parameter $(a, 1 - e)$ can be overplotted on the figure to estimate the parameter measurement errors in a similar way. Moreover, Figure 3 indicates that our analysis of the parameter measurement accuracy is robust to variations in simulation results. For example, in panels (a) and (b), regions with SNR > 1 (to the left of the dashed line at SNR = 1) show $\delta f_{\mathrm{orb}}/f_{\mathrm{orb}} \lesssim 10^{-5}$ and $\delta e/e \lesssim 10\%$. This suggests that, in realistic observations, BBH systems detected in the Milky Way GCs can typically achieve high-accuracy measurements of f_{orb} and e. Furthermore, as shown in panel (c), BBHs with SNR > 20 can have a mass measurement accuracy of $\delta M/M \lesssim 10\%$. However, marginally detectable sources may have poorly constrained total mass (blue regions near the dashed line of SNR = 5). Similarly, panel (d) shows that BBHs with SNR > 20 can have a sky localization accuracy of $2a_s \lesssim 300'$ (yellow regions), which indicates that high-SNR BBHs can generally be localized with an angular resolution of a few degrees in the Milky Way.

In Figure 4, we summarize all BBHs with SNR > 3 (assuming a 5 yr observation) from the simulation and compute their exact parameter measurement errors. These BBHs are drawn from 10

realizations in total, excluding the ejected population owing to the poor constraints on their location within the Milky Way. In particular, the top panel shows the relative errors in orbital frequency and eccentricity measurements, the middle panel shows the relative error in total mass and mass ratio measurements, and the bottom panel shows the absolute error in the distance (x-axis) and sky localization (y-axis) measurements. In each panel, we use different colors to show the SNR of BBHs and the shape to show the eccentricity ($e > 0.7$, plotted in triangles; $e < 0.7$, plotted in circles). Additionally, we exclude the parameter space where measurement accuracy is insufficient for astrophysical interpretation, as marked using gray shaded regions. Specifically, in the middle panel, regions with $\delta M/M > 50\%$ and $\delta q/q > 100\%$ are excluded, as the BBHs in these regions are indistinguishable from other compact binary sources, such as binary neutron stars (BNSs) or double white dwarfs (DWDs). Similarly, in the bottom panel, BBHs with $2a_s > 1000'$ ($\sim$5–10 times the typical tidal radius of the Milky Way GCs) and $\delta R > 200\,\mathrm{kpc}$ (halo radius of the Milky Way) cannot be confidently localized within a Milky Way GC.

As shown in the top panel, most detectable BBHs in Milky Way GCs have well-constrained orbital frequency and eccentricity. In particular, the fractional error in orbital frequency, $\delta f_{\mathrm{orb}}/f_{\mathrm{orb}}$, reaches an accuracy of $\sim 10^{-7}$ to 10^{-5} for BBHs with SNR > 3, which indicates a frequency resolution of $\delta f_{\mathrm{orb}} \lesssim 10^{-10}\,\mathrm{Hz}$ in LISA data analysis (see, e.g., Equation (18) in Z. Xuan et al. 2025, for an analytical explanation). Furthermore, all sources in Figure 4 have eccentricity measurement errors below $\delta e/e < 1$, which allows us to confidently detect nonzero eccentricities and distinguish dynamically formed BBHs from circular binaries created via isolated evolutionary channels. Additionally, highly eccentric sources typically exhibit higher accuracy in eccentricity measurement, with $\delta e/e$ reaching $\sim$0.1%–10% for BBHs with $e > 0.7$. This trend is consistent with the results of our previous works (Z. Xuan et al. 2023), which shows that eccentricity can break the degeneracy of waveform and significantly enhance the parameter measurement. In general, accurate measurements of orbital frequency and eccentricity can provide valuable insights into the long-term evolution of BBHs, enable the detection of potential environmental effects, and help infer different formation channels.

On the other hand, mHz GW detection may be less sensitive to the mass of BBHs in the Milky Way, primarily due to degeneracies in the waveform.[10] For example, most BBHs in the middle panel do not have a well-constrained mass ratio, with the relative error of measurement exceeding $\delta q/q \gtrsim 100\%$ (except for one highly eccentric BBH system with SNR $\sim$ 75, indicated by the red triangle in the lower left corner of the middle panel). However, the total mass measurement is sufficiently accurate for a significant fraction of detectable BBHs, reaching $\delta M/M \sim 1\%$–10% for sources with SNR $\gtrsim$ 20 (see the red and orange circles to the left of the dashed line). Therefore, we expect LISA to accurately measure the mass of these high-SNR BBHs in the Milky Way GCs, making them distinguishable from BNSs and DWDs.

Furthermore, we highlight that LISA can accurately localize most BBHs with SNR > 20 in Milky Way GCs (see the red and orange circles in the bottom panel). In particular, these GW sources have a sky localization accuracy of $\sim$10′–100′ (i.e., less

---

[9] We note that the parameter measurement accuracy in Figure 3 can be rescaled for BBHs with different distances; see Equation (14) in Z. Xuan et al. (2025) for more details.

[10] Note that we expect most detectable BBHs in the Milky Way to be long-living systems; thus, their orbital evolution is slow, and their chirp rate is hard to measure (see, e.g., Section 3.2 in Z. Xuan et al. 2024b).
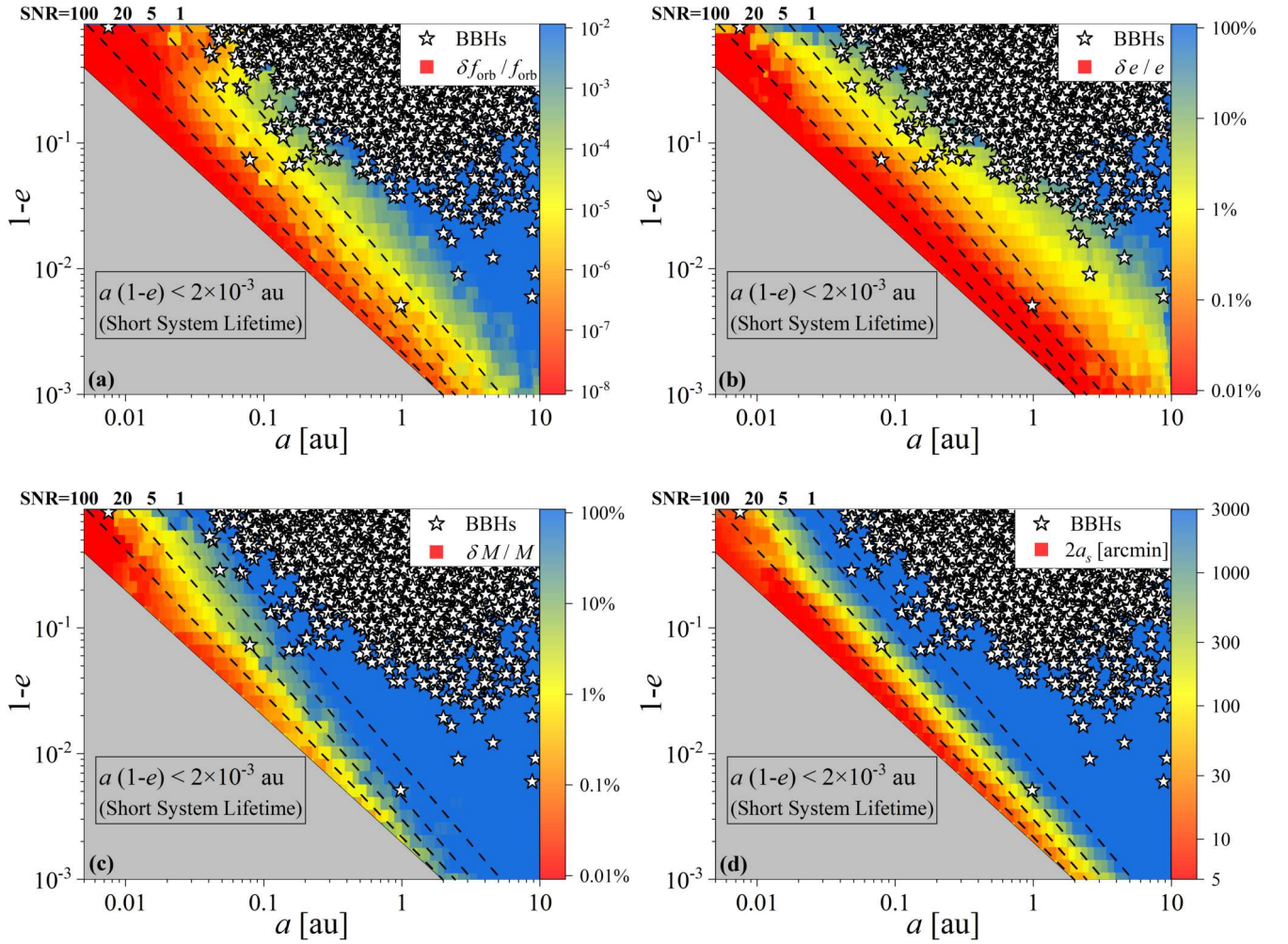
Figure 3. The population of BBHs from simulated Milky Way GCs, and their estimated parameter measurement error as a function of semimajor axis and eccentricity (for a 5 yr observation). Here we adopt the simulation result of the compact binary population in the Milky Way GCs (see Section 2; note that here we show a single realization of the in-cluster and ejected BBHs from Milky Way GCs) and plot the semimajor axis and eccentricity (as $1 - e$) of each BBH system (see the white stars). The background color maps the compact binary's parameter measurement error, for the orbital frequency ($\delta f_{\rm orb}/f_{\rm orb}$; panel (a)), eccentricity ($\delta e/e$; panel (b)), total mass ($\delta M/M$; panel (c)), and sky location (major axis of sky error ellipsoid, $2a_s$; panel (d)). We note that, in reality, the BBHs can have different mass, inclination, and sky locations, which affects their parameter measurement. However, for simplicity, here we assume fixed intrinsic parameters of $m_1 = 10\,M_\odot$, $m_2 = 15\,M_\odot$, $R = 8$ kpc, and $\Phi = \Theta = \theta = \phi = \psi = \pi/4$ when estimating the Fisher matrix and mapping the parameter measurement accuracy. In each panel, the dashed lines represent equal SNR contours (analytically calculated using Equation (2)), with SNR = 1, 5, 20, 100 from right to left. We exclude the parameter space where the binary has a pericenter distance smaller than $a\,(1 - e) < 2 \times 10^{-3}$ au, since they have a short merger timescale and negligible number expectation in our simulation.

than a few degrees), which is comparable to the typical diameter of Milky Way GCs ($\sim 10'$–$120'$).[11] Additionally, while the distance of BBHs is less precisely constrained compared to their sky location, most systems with SNR > 20 have a distance measurement error of $\delta R \sim 1$–100 kpc in the Milky Way. Given the significant distance to the nearby galaxies (e.g., the Andromeda galaxy is located at ~ 780 kpc), we expect these BBHs to be distinguishable from extragalactic GW sources.

### 3.4. Further Validation of BBH Localization Using Bayesian Analysis

As shown by Section 3.3, LISA has the potential to confidently localize a BBH system in specific Milky Way GCs, which could provide unique information about the Milky

Way's compact binary formation and the dynamical environment of GCs. In this section, we further verify this point using a Bayesian analysis and address the uncertainty introduced by the BBHs' distance measurement.

First, we note that although the Fisher matrix analysis adopted in Section 3.3 has been widely used to estimate the parameter measurement error for LISA sources, this method can sometimes yield inaccurate results, particularly for degenerate parameters or parameters with weak influences on the shape of GW signal (see, e.g., M. Vallisneri 2008; A. Toubiana et al. 2020). Consequently, the parameter measurement accuracy presented in Figures 3 and 4 should be interpreted as a heuristic estimation. Nevertheless, these estimates provide compelling evidence that BBHs in Milky Way GCs are promising targets for inferring their astrophysical properties.

To further validate the Fisher matrix results, we performed a full 10-dimensional Bayesian analysis for individual systems (see, e.g., L. S. Finn 1992; C. Cutler & É. E. Flanagan 1994; N. Christensen & R. Meyer 1998, 2001), as shown in Figure 5

---

[11] Note that detectable BBHs are more likely to be hosted by nearby, massive GCs (see Section 3.2); as a result, their host clusters tend to have larger angular sizes than the general Milky Way GC population. For BBHs with SNR > 1, the average host GC diameter is $\sim 38'$ (see Figure 6 in the Appendix).
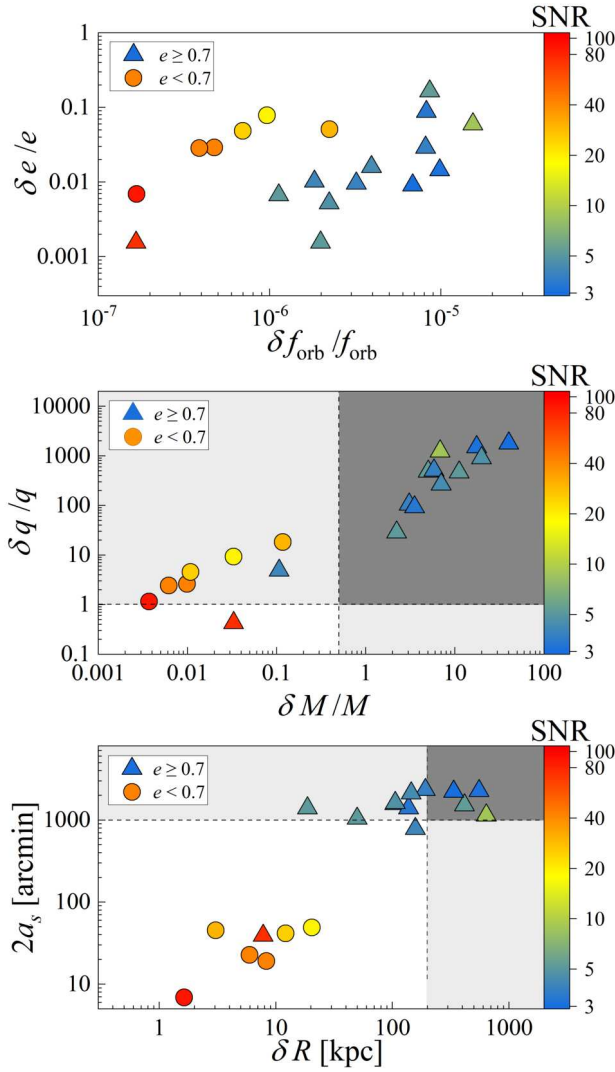
Figure 4. Parameter measurement error of the detectable BBHs in simulated Milky Way GCs, estimated using Fisher matrix analysis. Here we adopt the simulation results of the BBH population in Milky Way GCs, with a total of 10 realizations. Each point in the figure represents a BBH system in the simulation, with the color showing the SNR of its GW signal (assuming a 5 yr observation) and the shape showing the eccentricity of the orbit ($e > 0.7$, plotted in triangles; $e < 0.7$, plotted in circles). The top panel shows the relative error of orbital frequency and eccentricity measurement. The middle panel shows the relative error of total mass and mass ratio measurement. In the bottom panel, we show the absolute error of the BBHs' distance measurement (x-axis) and their sky localization accuracy (as the major axis of the sky error ellipsoids, $2a_s$, on the y-axis). We exclude the parameter space where measurement accuracy is insufficient to help with the astrophysical interpretation, as marked using gray shaded regions.

and Table 1. Particularly, in Figure 5 we choose an example BBH system from the simulation results ($m_1 = 23.3$ $M_\odot$, $m_2 = 18.6 M_\odot$, $a = 0.06332$ au, $e = 0.897$, $R = 4.9$ kpc) and inject its GW signal $s_0(t;\lambda)$[12] into a simulated stationary Gaussian LISA noise $n(t)$, which yields the mock LISA signal:

$$z(t) = s_0(t; \lambda) + n(t). \quad (10)$$

We then adopted Monte Carlo sampling, generating GW templates $s(t; \lambda)$ with parameters slightly different from their

intrinsic values of λ and computing their inner product with the mock signal (see Equation (6)):

$$\langle z|s \rangle = 2 \int_0^\infty \frac{\tilde{z}(f)\tilde{s}^*(f) + \tilde{z}^*(f)\tilde{s}(f)}{S_n(f)} df. \quad (11)$$

Assuming a uniform hyperrectangular prior, the posterior probability density of the observed parameters can be computed using the aforementioned inner products (see, e.g., Equations (1)–(6) in N. Christensen & R. Meyer 2001):

$$p(\lambda'|z) \propto p(z|\lambda')$$
$$= K \exp[2\langle z|s(\lambda')\rangle - \langle s(\lambda')|s(\lambda')\rangle], \quad (12)$$

where K is a constant.

As shown in Figure 5, the marginal posterior density of the binary's observed parameters, as indicated by the color maps, yields a parameter measurement error comparable to the Fisher matrix estimation. Particularly, the Fisher matrix estimation of this example BBH system is represented by the red triangle in the lower left corner of each panel in Figure 4, with its parameter measurement error $\delta f_{orb} \sim 2.1 \times 10^{-12}$ Hz, $\delta e \sim 1.4 \times 10^{-3}$, $\delta M \sim 1.4 M_\odot$, $\delta R \sim 7.8$ kpc, and sky localization accuracy $2a_s \sim 39' \sim 0°.65$. These values are generally consistent with the 1σ levels in Bayesian analysis, which yields $\delta f_{orb} \sim 2.8 \times 10^{-12}$ Hz, $\delta e \sim 1.2 \times 10^{-3}$, $\delta M \sim 3.1 M_\odot$, $\delta R \sim 1.1$ kpc, and sky localization accuracy $\sim 1°.3$ (see Figure 5). Therefore, the Bayesian study of this specific case partly justifies the Fisher matrix results of Figures 3 and 4. We also show the Bayesian analysis results of a BBH with SNR ~ 9 (see Figure 7 in the Appendix), which validates the parameter measurement accuracy for sources in the marginal detection case.

Using the aforementioned method, we showcase three representative systems from the mock Milky Way GC catalog, with $e = 0.1671$–0.8969 (see Table 1 in the Appendix). To better describe the sources' localization accuracy, we convert the posterior of their sky location angles, (ϕ, θ), into the solid angle of the corresponding sky area $\delta\Omega_{Bayesian}$ (68% credible region). We then compare $\delta\Omega_{Bayesian}$ with the area of sky error ellipsoid from Fisher matrix analysis, $\delta\Omega_{Fisher}$, and the size of their host GCs. As shown in Table 1, the Fisher matrix and Bayesian analysis generally yield consistent results in the sources' sky localization accuracy, although the Fisher results are systematically smaller by a factor of ~ 2 in angular size estimation (or ~ 5 in sky area). Furthermore, for high-SNR BBHs (see, e.g., the three systems with SNR = 35–94 in Table 1), their sky area accuracies, as estimated from both Fisher matrix and Bayesian analysis ($\sim 0.40, 1.00, 1.85$ deg^2), are comparable with (or even smaller than) the size of their host clusters, $\sim 2.84, 2.13, 0.52$ deg^2.[13] These results further confirm that BBHs in the Milky Way can be localized to the sky area of specific host GCs, especially for significant detection cases.

Notably, Figures 4 and 5 and Table 1 indicate a distance measurement error of $\delta R \sim 1$–100 kpc for the Milky Way BBH sources, which is much larger than the tidal diameter of GCs (typically on the order of a few tens of parsecs). Therefore, LISA is unlikely to directly associate the spatial position of a BBH system with its host GC because of the large uncertainty

---

[12] Note that this system has SNR ~ 77 for a 5 yr observation, and the detector response function is included in $s_0(t)$; see Section 3.3.

[13] However, marginally detectable BBHs (SNR ~ 8) can have poor sky localization. For example, the system in Figure 7 has a sky localization error of ~ 233 deg^2 in Bayesian analysis, far exceeding the angular size of its host cluster NGC 7078 (~ 0.39 deg^2).
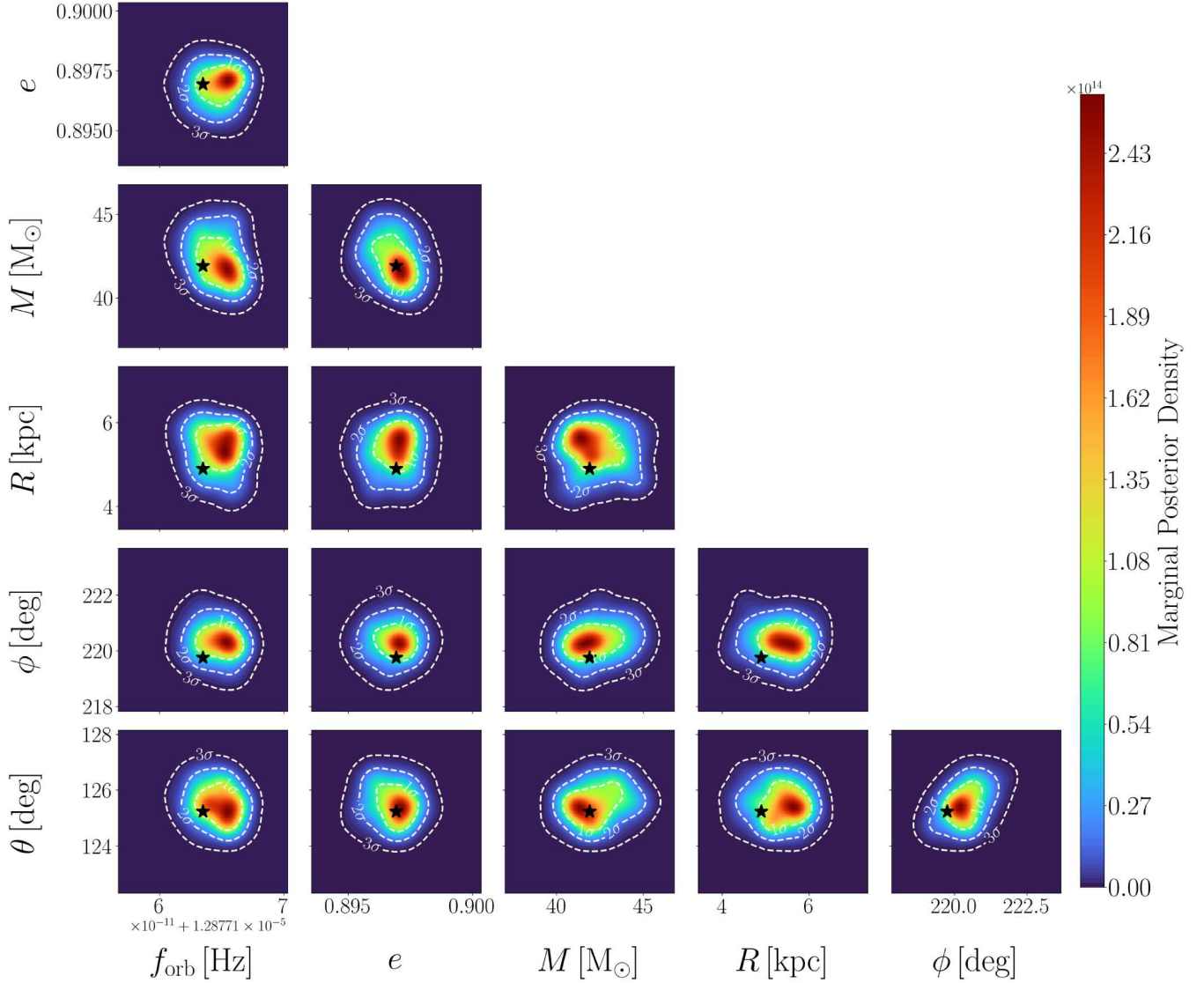
Figure 5. Parameter measurement error of an example BBH system in Milky Way GCs, estimated using Bayesian analysis (for a 5 yr observation). Here we consider a BBH system with $m_1 = 23.3\,M_\odot$, $m_2 = 18.6\,M_\odot$, $f_{\rm orb} = 1.2877164 \times 10^{-5}$ Hz, $e = 0.897$, $R = 4.9$ kpc, $\Phi = 158°.7$, $\Theta = 141°.4$, $\phi = 219°.9$, $\theta = 125°.2$, $\psi = 153°.9$. (Note that this system has SNR ~ 77, and we keep eight significant digits of $f_{\rm orb}$ to highlight its realistic measurement accuracy.) The color maps show the marginal posterior density of the binary's observed parameters, assuming a flat, 10-dimensional hyperrectangular prior and stationary Gaussian LISA noise. We use the star in each panel to indicate the system's intrinsic parameters, and we plot 68%, 95%, and 99.7% credible regions for the marginal posterior densities (i.e, 1σ -3σ level sets defined analogously to a bivariate Gaussian density). To avoid clutter, we plot the results for the binary's intrinsic parameters $f_{\rm orb}$, e, M; distance R; and sky location ϕ, θ, which are mostly relevant to its astrophysical inference. Additionally, the peak of posterior density exhibits a small offset from some parameters' intrinsic value (typically within the 1σ level), which is caused by the random fluctuation of time-domain LISA noise and the limit of numerical accuracy for highly eccentric binary waveforms.

in the radial distance measurement. However, when determining the host environment of BBH sources, this uncertainty can be resolved, mostly because stellar density in the Milky Way halo is much lower than that of GCs. In other words, the total number of stars in a BBH-hosting GC ($\sim 10^5$–10^6; see Figure 2) is much larger than the total number of halo stars in other parts of the error volume,[14] which makes it highly possible that a detected source is hosted in the cluster instead of other regions of the local Universe.

For example, assuming a halo stellar mass density of $\rho_{\rm halo} \sim 10^{-4}\,M_\odot\,{\rm pc}^{-3}$ (A. J. Deason et al. 2019), the total halo

stellar mass in the error volume $V_{\rm err}$ of GW detection can be estimated as

$$M_{\rm halostars} = \rho_{\rm halo} \times V_{\rm err} \sim \rho_{\rm halo} {\rm R}^2 \delta {\rm R} \delta \Omega_{\rm Bayesian}, \qquad (13)$$

which yields $M_{\rm halostars} \sim 51\,M_\odot$, $1.5 \times 10^3\,M_\odot$, $6.5 \times 10^4\,M_\odot$ for the first three confidently localized systems in Table 1. These values are much smaller than the total stellar mass of their host GCs, which is estimated as $M_{\rm GC} \sim 7 \times 10^5\,M_\odot$, $1.5 \times 10^6\,M_\odot$, $2 \times 10^5\,M_\odot$ for NGC 104, NGC 5139, and NGC 6341, respectively (see, e.g., M. Marks & P. Kroupa 2010).

We note that the relative contributions of GCs and the Galactic field to the total BBH merger rate remain uncertain

---

[14] Note that most GCs reside in the Galactic halo (see, e.g., W. E. Harris 2010).

(see I. Mandel & F. S. Broekgaarden 2022, for a review). However, recent studies suggest that both are likely contributing at a comparable rate (see, e.g., M. Zevin et al. 2021a; M. Fishbach & G. Fragione 2023). Furthermore, even if the Galactic field has a larger contribution to the total merger rate, considering the significant difference in total stellar mass between the field ($\sim 10^{10} M_\odot$ for the Milky Way; M. Cautun et al. 2020) and GCs ($\sim 10^7 M_\odot$ for the Milky Way; W. E. Harris 2010), the BBH merger rate per unit stellar mass in GCs is likely comparable to or higher than that in the field. Thus, we assume that all stellar mass (in the Galactic halo and in GCs) has an equal probability of hosting a BBH source. Under this assumption, the probability that a given BBH resides in a GC can be estimated as

$$P_{\text{incluster}} \sim \frac{M_{\text{GC}}}{M_{\text{GC}} + M_{\text{halostars}}}. \tag{14}$$

Therefore, once a source is accurately located in the sky area of a GC, the probability for the system to be a GC BBH source can be significantly boosted, especially because a GC contributes to the majority of stellar mass in the error volume. Additionally, the highly eccentric formation nature of BBHs in GC (see, e.g., Section 3.1) can also help with distinguishing them from other BBHs from isolated evolution channels in the Galactic field, which are expected to have negligible eccentricities (e.g., K. Belczynski et al. 2016; S. Stevenson et al. 2017; J. J. Eldridge et al. 2019).[15]

4. Discussion

In this work, we explore the realistic detectability and parameter measurement accuracy of BBHs in Galactic GCs for observations with LISA. Particularly, since GCs are considered ideal environments for the dynamical formation of BBHs (see, e.g., M. C. Miller & D. P. Hamilton 2002; C. L. Rodriguez et al. 2015; J. Samsing 2018), constraining their detectability potential is of prime importance for the community. Notably, K. Kremer et al. (2018a) predicted that LISA might detect a significant number of BBH sources from ~ 150 GCs in the Milky Way, with various orbital parameters. Furthermore, many dynamically formed BBHs can undergo a wide ($a \gtrsim 0.1$ au), highly eccentric ($e \gtrsim 0.9$) progenitor phase before merger (B. Kocsis & J. Levin 2012a; B.-M. Hoang et al. 2019; Z. Xuan et al. 2024b, 2024a, 2025; A. M. Knee et al. 2024), which has been recently proposed to have unique imprints on the mHz GW detection. By detecting these eccentric sources, we can distinguish between different formation mechanisms (W. E. East et al. 2013; J. Samsing et al. 2014; M. Coughlin et al. 2015; K. Breivik et al. 2016; S. Vitale 2016; A. Nishizawa et al. 2017; M. Zevin et al. 2017, 2021a; L. Gondán et al. 2018b, 2018a; M. E. Lower et al. 2018; C. J. Moore et al. 2019; I. M. Romero-Shaw et al. 2019; R. Abbott et al. 2021; The LIGO Scientific Collaboration et al. 2023), enhance the parameter measurement accuracy (such as the orbital frequency evolution and source location; see Z. Xuan et al. 2023, 2025), and probe the potential presence of tertiary companions through eccentricity

oscillations (T. A. Thompson 2011; J. M. Antognini et al. 2014; B.-M. Hoang et al. 2018, 2020; A. P. Stephan et al. 2019; M. A. S. Martinez et al. 2020; S. Naoz et al. 2020; H. Wang et al. 2021; A. M. Knee et al. 2022).

Using the CMC Cluster Catalog of K. Kremer et al. (2020), we generate a best-fit model for each Milky Way GC,[16] and we estimate the BBH population within these clusters (illustrated in Figure 1). We then generate the BBHs' GW signals using the x-model (I. Hinder et al. 2010), which incorporates the dynamics of eccentric compact binaries up to 3 PN order. Additionally, the waveform analysis includes the detector's annual motion around the Sun so that our results can represent the realistic detection of GW signals. More details of the waveform model and analysis method can be found in Z. Xuan et al. (2025).

Based on the simulation, we compute the number of detectable BBHs formed in Galactic GCs (see Section 3.1). In total, we expect the GW signal from 0.7 ± 0.7, 2.0 ± 1.7, 3.6 ± 2.3, and 13.4 ± 4.7 BBHs to exceed the threshold of SNR $= 30$, 5, 3, and 1, respectively, for a 10 yr observation of LISA. Among all these sources, in-cluster BBHs contribute to 0.7, 1.5, 2.2, and 5.8 GW sources, and the ejected population contributes to ~ 0, 0.5, 1.4, and 7.6 GW sources above the threshold of SNR $= 30$, 5, 3, and 1, respectively. We highlight that $\sim 50\%$ of the BBHs with SNR > 5 have high eccentricity in the detection ($e \gtrsim 0.9$), which reflects the dominant population of eccentric BBHs in GCs (as they are long-living sources; see, e.g., Equation (4)) and indicates that most of the GW signals from BBHs in Milky Way GCs are characterized by highly eccentric "GW bursts" in future LISA detection (see, e.g., Z. Xuan et al. 2024b).

Furthermore, we analyze the properties of Galactic GCs that are most likely to host resolvable LISA sources (see Figure 2). Specifically, we calculate the expected probability for a cluster to host a BBH system with SNR > 1 during a 10 yr LISA observation. As shown in Figure 2, these BBH-hosting GCs tend to cluster within specific regions of the parameter space, where the GCs have a close distance to the detector ($R \lesssim 10$ kpc), exhibit a small r_c/r_h (~ 0.1–0.3), and have a large total mass.

To evaluate the measurement accuracy achievable with LISA, we performed a Fisher matrix analysis on the simulated BBH population, as illustrated in Figures 3 and 4. Particularly, Figure 3 maps the intrinsic parameters, $(a, 1 - e)$, of the simulated Milky Way GC BBH population and uses the background color to show their different parameter measurement errors (5 yr observation); Figure 4 depicts the measurement error of $\{f_{\text{orb}}, e, M, q, R, 2a_s\}$ for all the simulated BBHs with SNR > 3, across all 10 realizations, for a 5 yr observation. As illustrated in both figures, most of the BBHs with SNR > 3 have well-constrained orbital frequency and eccentricity, reaching $\delta f_{\text{orb}}/f_{\text{orb}} \sim 10^{-7}$ to 10^{-5} and $\delta e/e < 1$. Furthermore, eccentricity can, in general, enhance the measurement accuracy, with $\delta e/e$ reaching $\sim 10^{-3}$ to 0.1 for detectable BBHs with $e > 0.7$. On the other hand, BBHs with SNR > 20 can have a total mass measurement accuracy of $\delta M/M \lesssim 10\%$, but most of the marginally detectable sources may not have a well-constrained total mass and mass ratio. In addition, we expect BBHs with SNR > 20 to be confidently

---

[15] However, the localization method discussed earlier in this section is agnostic to the expected eccentricity distributions of different BBH formation channels. For example, if a population of eccentric BBHs is accurately localized toward the Galactic field rather than any GCs, this method can also distinguish it from the in-cluster BBH population.

[16] Which is computed using the Monte Carlo N-body dynamics code CMC.

localized with an angular resolution of $\sim 10'$–$100'$, which enables us to localize these sources in specific Milky Way GCs.

In Section 3.4, we adopt Bayesian analysis to verify the localization accuracy of BBH sources. As shown in Figure 5 and Table 1, the full 10-dimensional Bayesian analysis for individual BBH sources yields parameter measurement errors (at the 1σ levels of the marginal posterior distributions) that are consistent with those from Fisher matrix analysis, within one order of magnitude. Notably, Table 1 presents localization results for representative systems from the mock Milky Way GC catalog. For BBHs with SNR = 35, 77, and 94, the typical sky localization errors exhibit similar values ($\sim 1\,\mathrm{deg}^2$) compared to their host cluster size. This result further confirms LISA's potential to confidently localize BBHs within individual Galactic GCs. Additionally, Milky Way BBH sources typically have large uncertainty in their radial distance measurement (~ 1–$100\,\mathrm{kpc}$). However, as shown in Equations (13)–(14), once a BBH is localized within the sky area of a GC, the probability of its cluster origin is significantly enhanced owing to the large number of stars in GCs ($\sim 10^5$–10^6 stars) compared to the stars within the rest of the error volume (i.e., the low-density Galactic halo).

Although our collective sample of GC simulations effectively spans the full parameter space of Galactic GCs (K. Kremer et al. 2020), this simulation suite is a grid, which inevitably means that some specific observed GCs do not necessarily have a strong "one-to-one" model match. For example, N. Z. Rui et al. (2021) demonstrated how the CMC Catalog may be augmented with additional models to match particular GCs with observed properties lying in between grid points. In another recent study, C. S. Ye et al. (2022) showed that especially massive GCs like 47 Tuc (NGC 104) may require additional adjustments (in particular, variations to the initial density profile and initial stellar mass function) to produce a precise model match. The ideal solution is to produce a separate model for every single Galactic cluster (for some examples, see K. Kremer et al. 2018b, 2019a; C. S. Ye et al. 2022, 2024); however, this is computationally expensive and outside the scope of the current study. We tested the LISA predictions from our best-fit model for NGC 104 with the predictions from the more precise model in C. S. Ye et al. (2022) and found that the number of LISA sources is consistent within a factor of 3 for SNR > 1. Furthermore, the multimodality of the posterior, particularly in angular parameters, can pose additional challenges for accurate sky localization (see, e.g., S. Marsat et al. 2021). However, a comprehensive analysis of this effect is beyond the scope of the present work.

Additionally, this work simulates the BBH population in observed GCs of the Milky Way, which does not include other potential GW sources in the local galaxy, such as BBHs formed in the Galactic nucleus, Galactic field, and evaporated GCs. Thus, the number expectation presented here only serves as a lower bound for the LISA detection. Notably, the high computational cost of N-body simulation limits the sample size presented in this Letter (in total 10 realizations), which may result in uncertainty of the predicted BBH population. However, the prediction of source number and parameter measurement accuracy in this work is expected to be a realistic estimation, based on one of the most up-to-date simulations of GCs (K. Kremer et al. 2020). In addition, the population properties presented here agree with previous works with different GC models (see, e.g., K. Kremer et al. 2018a), which indicates the robustness of the result that LISA can detect a handful of BBHs formed in the Milky Way GCs.

To conclude, mHz-frequency BBHs in Milky Way GCs have the potential to enable a direct test of the role of GCs in the formation of GW sources. Given a 5–10 yr LISA observation, these systems typically have highly resolved orbital frequency ($\delta f_{\mathrm{orb}}/f_{\mathrm{orb}} \sim 10^{-7}$ to 10^{-5}) and eccentricity ($\delta e/e \sim 10^{-3}$ to 0.1), as well as a measurable total mass when the SNR exceeds ~ 20. Furthermore, these high-SNR BBHs can be confidently localized in a specific GC of the Milky Way, with an angular resolution of $\sim 10'$–$100'$ in the sky. Therefore, we highlight the potential of detecting BBHs in Milky Way GCs, which allows for accurate tracking of their long-term orbital evolution, distinguishing the compact binary formation mechanisms, and understanding the properties of GCs in the local galaxy.
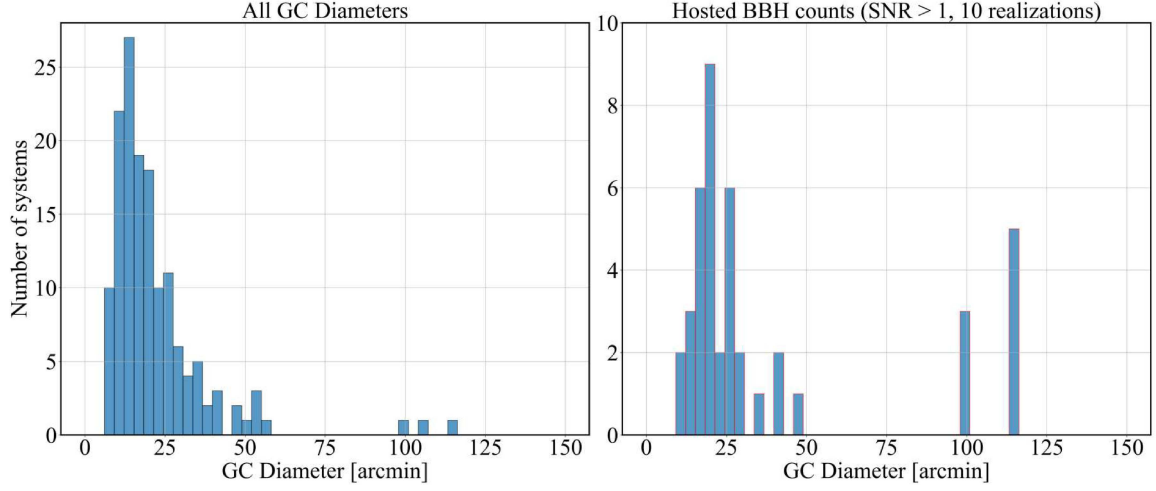
Appendix

In this section, we present the histogram of angular diameters for Milky Way globular clusters (Figure 6), the parameter measurement errors for an example BBH system in the Milky Way (Figure 7), and the sky localization and distance measurement accuracies for representative systems in the mock Milky Way GC catalog (Table 1).

Figure 6. Histogram of Milky Way GC angular diameters and their hosted BBH counts. Here we show the distribution of GC angular diameters (left), taken from the Milky Way Star Clusters Catalog (N. V. Kharchenko et al. 2012, 2013; S. Schmeja et al. 2014; R. D. Scholz et al. 2015), and the number of hosted BBH systems with SNR > 1 in each GC diameter bin (right), based on 10 realizations from the `CMC Cluster Catalog`. The difference between the left and right panels arises because detectable BBH systems tend to be hosted by more massive and nearby GCs, which also have a larger angular size.
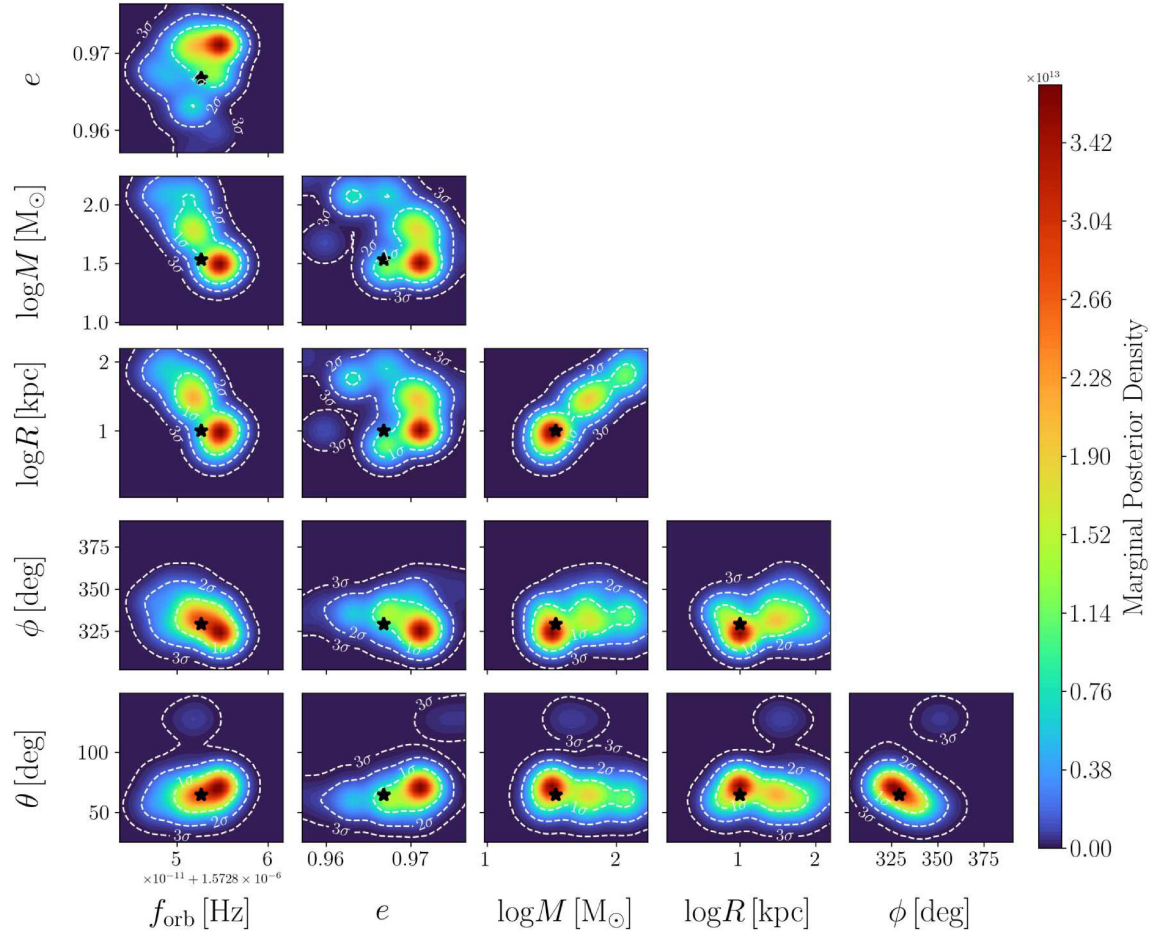
Figure 7. Parameter measurement error of an example BBH system in Milky Way GCs. Here we adopt the same method as in Figure 5, but we consider a different BBH system with $m_1 = 17.6\ M_\odot$, $m_2 = 16.5\ M_\odot$, $f_{\rm orb} = 1.572852 \times 10^{-6}$ Hz, $e = 0.9668$, $R = 10$ kpc, $\Phi = 329°.2$, $\Theta = 64°.5$, $\phi = 341°.4$, $\theta = 149°.8$, $\psi = 14°.8$ (SNR ~ 9).

Table 1
Sky Location and Distance Measurement Accuracy of Representative Systems in the Mock Milky Way GC Catalog, Compared with Their Host Cluster Size (5 yr Observation)

Host Cluster	Cluster Size (deg^2)	$\delta\Omega_{\text{Bayesian}}$ (deg^2)	$\delta\Omega_{\text{Fisher}}$ (deg^2)	δR (kpc)	M ($M_\odot$)	a (au)	e	SNR (5 yr)
NGC 104	2.84	0.40	0.073	0.25	29.5	0.01102	0.2803	94
NGC 5139	2.13	1.00	0.17	2.16	41.9	0.06332	0.8969	77
NGC 6341	0.52	1.85	0.38	18.0	21.2	0.00750	0.1671	35

Note. Here $\delta\Omega_{\text{Bayesian}}$ represents the sky area of 68% credible regions of the marginal posterior densities (see, e.g., the bottom right panel of Figure 5); $\delta\Omega_{\text{Fisher}} = \pi a_s b_s$ represents the area of sky error ellipsoid, as estimated by Fisher matrix analysis; δR shows the distance measurement accuracy, as of 3σ level from Bayesian analysis; M, a, and e represent the total mass, semimajor axis, and eccentricity of the binary system, respectively. For comparison purposes, we show the name and sky area of each binary's host cluster (inferred from their angular radius in the Milky Way Star Clusters Catalog; N. V. Kharchenko et al. 2012, 2013; S. Schmeja et al. 2014; R. D. Scholz et al. 2015).

ORCID iDs

Zeyuan Xuan https://orcid.org/0000-0003-1356-0915
Kyle Kremer https://orcid.org/0000-0002-4086-3180
Smadar Naoz https://orcid.org/0000-0002-9802-9279

References

Aarseth, S. J. 2012, MNRAS, 422, 841
Abbott, R., Abbott, T. D., Acernese, F., et al. 2023, PhRvX, 13, 041039
Abbott, R., et al. 2021, ApJL, 913, L7
Amaro-Seoane, P., Audley, H., Babak, S., et al. 2017, arXiv:1702.00786
Amaro-Seoane, P., Andrews, J., Sedda, M. A., et al. 2023, LRR, 26, 2
Antognini, J. M., Shappee, B. J., Thompson, T. A., & Amaro-Seoane, P. 2014, MNRAS, 439, 1079
Antonini, F., & Gieles, M. 2020a, MNRAS, 492, 2936
Antonini, F., & Gieles, M. 2020b, PhRvD, 102, 123016
Arca Sedda, M., Askar, A., & Giersz, M. 2018, MNRAS, 479, 4652
Arca Sedda, M., Naoz, S., & Kocsis, B. 2023, Univ, 9, 138
Barack, L., & Cutler, C. 2004, PhRvD, 69, 082005
Baumgardt, H., & Hilker, M. 2018, MNRAS, 478, 1520
Belczynski, K., Holz, D. E., Bulik, T., & O'Shaughnessy, R. 2016, Natur, 534, 512
Benacquista, M. J., Portegies Zwart, S., & Rasio, F. A. 2001, CQGra, 18, 4025
Bird, S., Cholis, I., Muñoz, J. B., et al. 2016, PhRvL, 116, 201301
Breen, P. G., & Heggie, D. C. 2013, MNRAS, 432, 2779
Breivik, K., Mingarelli, C. M. F., & Larson, S. L. 2020, ApJ, 901, 4
Breivik, K., Rodriguez, C. L., Larson, S. L., Kalogera, V., & Rasio, F. A. 2016, ApJL, 830, L18
Brown, D. A., & Zimmerman, P. J. 2010, PhRvD, 81, 024007
Cautun, M., Benítez-Llambay, A., Deason, A. J., et al. 2020, MNRAS, 494, 4291
Chen, X., Li, S., & Cao, Z. 2019, MNRAS, 485, L141
Christensen, N., & Meyer, R. 1998, PhRvD, 58, 082001
Christensen, N., & Meyer, R. 2001, PhRvD, 64, 022001
Chua, A. J. K., Katz, M. L., Warburton, N., & Hughes, S. A. 2021, PhRvL, 126, 051102
Coe, D. 2009, arXiv:0906.4123
Cornish, N. J., & Rubbo, L. J. 2003, PhRvD, 67, 022001
Coughlin, M., Meyers, P., Thrane, E., Luo, J., & Christensen, N. 2015, PhRvD, 91, 063004
Cutler, C. 1998, PhRvD, 57, 7089
Cutler, C., & Flanagan, É. E. 1994, PhRvD, 49, 2658
Deason, A. J., Belokurov, V., & Sanders, J. L. 2019, MNRAS, 490, 3426
D'Orazio, D. J., & Samsing, J. 2018, MNRAS, 481, 4775
Downing, J. M. B., Benacquista, M. J., Giersz, M., & Spurzem, R. 2010, MNRAS, 407, 1946
East, W. E., McWilliams, S. T., Levin, J., & Pretorius, F. 2013, PhRvD, 87, 043004
Eldridge, J. J., Stanway, E. R., & Tang, P. N. 2019, MNRAS, 482, 870
Fang, Y., Chen, X., & Huang, Q.-G. 2019, ApJ, 887, 210
Finn, L. S. 1992, PhRvD, 46, 5236
Fishbach, M., & Fragione, G. 2023, MNRAS, 522, 5546
Fragione, G., & Bromberg, O. 2019, MNRAS, 488, 4370
Gautham Bhaskar, H., Li, G., & Lin, D. 2023, arXiv:2303.12539
Gerosa, D., Ma, S., Wong, K. W. K., et al. 2019, PhRvD, 99, 103004
Gondán, L., Kocsis, B., Raffai, P., & Frei, Z. 2018a, ApJ, 855, 34
Gondán, L., Kocsis, B., Raffai, P., & Frei, Z. 2018b, ApJ, 860, 5
Harris, W. E. 1996, AJ, 112, 1487
Harris, W. E. 2010, arXiv:1012.3224
Heggie, D. C. 2001, arXiv:astro-ph/0111045
Hinder, I., Herrmann, F., Laguna, P., & Shoemaker, D. 2010, PhRvD, 82, 024033
Hoang, B.-M., Naoz, S., Kocsis, B., Farr, W. M., & McIver, J. 2019, ApJL, 875, L31
Hoang, B.-M., Naoz, S., Kocsis, B., Rasio, F. A., & Dosopoulou, F. 2018, ApJ, 856, 140
Hoang, B.-M., Naoz, S., & Kremer, K. 2020, ApJ, 903, 8
Huerta, E. A., Kumar, P., McWilliams, S. T., O'Shaughnessy, R., & Yunes, N. 2014, PhRvD, 90, 084016
Hughes, S. A., Warburton, N., Khanna, G., Chua, A. J. K., & Katz, M. L. 2021, PhRvD, 103, 104014
Katz, M. L., Chua, A. J. K., Speri, L., Warburton, N., & Hughes, S. A. 2021, PhRvD, 104, 064047
Kharchenko, N. V., Piskunov, A. E., Schilbach, E., Röser, S., & Scholz, R. D. 2012, A&A, 543, A156
Kharchenko, N. V., Piskunov, A. E., Schilbach, E., Röser, S., & Scholz, R. D. 2013, A&A, 558, A53
Klein, A., Barausse, E., Sesana, A., et al. 2016, PhRvD, 93, 024003
Knee, A. M., McIver, J., Naoz, S., et al. 2024, ApJL, 971, L38
Knee, A. M., Romero-Shaw, I. M., Lasky, P. D., McIver, J., & Thrane, E. 2022, ApJ, 936, 172
Kocsis, B., Haiman, Z., & Menou, K. 2008, ApJ, 684, 870
Kocsis, B., Haiman, Z., Menou, K., & Frei, Z. 2007, PhRvD, 76, 022003
Kocsis, B., & Levin, J. 2012a, PhRvD, 85, 123005
Kremer, K., Chatterjee, S., Breivik, K., et al. 2018a, PhRvL, 120, 191103
Kremer, K., Chatterjee, S., Ye, C. S., Rodriguez, C. L., & Rasio, F. A. 2019a, ApJ, 871, 38
Kremer, K., Rodriguez, C. L., Amaro-Seoane, P., et al. 2019b, PhRvD, 99, 063003
Kremer, K., Rui, N. Z., Weatherford, N. C., et al. 2021, ApJ, 917, 28
Kremer, K., Ye, C. S., Chatterjee, S., Rodriguez, C. L., & Rasio, F. A. 2018b, ApJL, 855, L15
Kremer, K., Ye, C. S., Rui, N. Z., et al. 2020, ApJS, 247, 48
Kroupa, P. 2001, MNRAS, 322, 231
Kulkarni, S. R., Hut, P., & McMillan, S. 1993, Natur, 364, 421
Lamberts, A., Garrison-Kimmel, S., Hopkins, P. F., et al. 2018, MNRAS, 480, 2704
Lang, R. N., & Hughes, S. A. 2006, PhRvD, 74, 122001
Lower, M. E., Thrane, E., Lasky, P. D., & Smith, R. 2018, PhRvD, 98, 083028
Mackey, A. D., Wilkinson, M. I., Davies, M. B., & Gilmore, G. F. 2007, MNRAS, 379, L40
Mandel, I., & Broekgaarden, F. S. 2022, LRR, 25, 1
Marks, M., & Kroupa, P. 2010, MNRAS, 406, 2000
Marsat, S., Baker, J. G., & Canton, T. D. 2021, PhRvD, 103, 083011
Martinez, M. A. S., Fragione, G., Kremer, K., et al. 2020, ApJ, 903, 67
Merritt, D., Piatek, S., Portegies Zwart, S., & Hemsendorf, M. 2004, ApJL, 608, L25
Michaely, E., & Naoz, S. 2022, ApJ, 936, 184
Michaely, E., & Perets, H. B. 2019, ApJL, 887, L36
Michaely, E., & Perets, H. B. 2020, MNRAS, 498, 4924
Mikóczi, B., Kocsis, B., Forgács, P., & Vasúth, M. 2012, PhRvD, 86, 104027
Miller, M. C., & Hamilton, D. P. 2002, ApJ, 576, 894

Moore, C. J., Gerosa, D., & Klein, A. 2019, MNRAS, 488, L94
Morscher, M., Pattabiraman, B., Rodriguez, C., Rasio, F. A., & Umbreit, S. 2015, ApJ, 800, 9
Muñoz, D. J., Stone, N. C., Petrovich, C., & Rasio, F. A. 2022, arXiv:2204.06002
Naoz, S. 2016, ARA&A, 54, 441
Naoz, S., & Haiman, Z. 2023, ApJL, 955, L27
Naoz, S., Rose, S. C., Michaely, E., et al. 2022, ApJL, 927, L18
Naoz, S., Will, C. M., Ramirez-Ruiz, E., et al. 2020, ApJL, 888, L8
Nishizawa, A., Sesana, A., Berti, E., & Klein, A. 2017, MNRAS, 465, 4375
O'Leary, R. M., Kocsis, B., & Loeb, A. 2009, MNRAS, 395, 2127
Peng, P., & Chen, X. 2021, MNRAS, 505, 1324
Peters, P. C., & Mathews, J. 1963, PhRv, 131, 435
Peuten, M., Zocchi, A., Gieles, M., Gualandris, A., & Hénault-Brunet, V. 2016, MNRAS, 462, 2333
Portegies Zwart, S. F., & McMillan, S. L. W. 2002, ApJ, 576, 899
Robson, T., Cornish, N. J., & Liu, C. 2019, CQGra, 36, 105011
Robson, T., Cornish, N. J., Tamanini, N., & Toonen, S. 2018, PhRvD, 98, 064012
Rodriguez, C. L., Amaro-Seoane, P., Chatterjee, S., et al. 2018, PhRvD, 98, 123005
Rodriguez, C. L., Chatterjee, S., & Rasio, F. A. 2016a, PhRvD, 93, 084029
Rodriguez, C. L., Haster, C.-J., Chatterjee, S., Kalogera, V., & Rasio, F. A. 2016b, ApJL, 824, L8
Rodriguez, C. L., Morscher, M., Pattabiraman, B., et al. 2015, PhRvL, 115, 051101
Rodriguez, C. L., Weatherford, N. C., Coughlin, S. C., et al. 2022, ApJS, 258, 22
Rom, B., Linial, I., Kaur, K., & Sari, R. 2024, ApJ, 977, 7
Romero-Shaw, I. M., Lasky, P. D., & Thrane, E. 2019, MNRAS, 490, 5210
Rui, N. Z., Kremer, K., Weatherford, N. C., et al. 2021, ApJ, 912, 102
Samsing, J. 2018, PhRvD, 97, 103014
Samsing, J., Bartos, I., D'Orazio, D. J., et al. 2022, Natur, 603, 237
Samsing, J., & D'Orazio, D. J. 2019, PhRvD, 99, 063006
Samsing, J., Hamers, A. S., & Tyles, J. G. 2019, PhRvD, 100, 043010
Samsing, J., MacLeod, M., & Ramirez-Ruiz, E. 2014, ApJ, 784, 71
Sasaki, M., Suyama, T., Tanaka, T., & Yokoyama, S. 2016, PhRvL, 117, 061101
Schmeja, S., Kharchenko, N. V., Piskunov, A. E., et al. 2014, A&A, 568, A51
Scholz, R. D., Kharchenko, N. V., Piskunov, A. E., Röser, S., & Schilbach, E. 2015, A&A, 581, A39
Sesana, A., Lamberts, A., & Petiteau, A. 2020, MNRAS, 494, L75
Sigurdsson, S., & Hernquist, L. 1993, Natur, 364, 423

Spitzer, L., J. 1969, ApJL, 158, L139
Stegmann, J., Vigna-Gómez, A., Rantala, A., et al. 2024, ApJL, 972, L19
Stephan, A. P., Naoz, S., Ghez, A. M., et al. 2019, ApJ, 878, 58
Stevenson, S., Vigna-Gómez, A., Mandel, I., et al. 2017, NatCo, 8, 14906
Tagawa, H., Kocsis, B., Haiman, Z., et al. 2021, ApJL, 907, L20
Tamanini, N., Klein, A., Bonvin, C., Barausse, E., & Caprini, C. 2020, PhRvD, 101, 063002
Tang, P., Eldridge, J. J., Meyer, R., et al. 2024, MNRAS, 534, 1707
The LIGO Scientific Collaboration, the Virgo Collaboration, the KAGRA Collaboration, et al. 2023, PhRvX, 13, 011048
Thompson, T. A. 2011, ApJ, 741, 82
Torres-Orjuela, A., Amaro Seoane, P., Xuan, Z., et al. 2021, PhRvL, 127, 041102
Toubiana, A., Marsat, S., Babak, S., Barausse, E., & Baker, J. 2020, PhRvD, 101, 104038
Vallisneri, M. 2008, PhRvD, 77, 042001
Vitale, S. 2016, PhRvL, 117, 051102
Vitale, S. 2021, Sci, 372, eabc7397
Vitale, S., & Whittle, C. 2018, PhRvD, 98, 024029
Wagg, T., Broekgaarden, F. S., de Mink, S. E., et al. 2022, ApJ, 937, 118
Wang, H., Stephan, A. P., Naoz, S., Hoang, B.-M., & Breivik, K. 2021, ApJ, 917, 76
Wang, L., Spurzem, R., Aarseth, S., et al. 2016, MNRAS, 458, 1450
Wen, L. 2003, ApJ, 598, 419
Winter-Granić, M., Petrovich, C., & Peña-Donaire, V. 2024, ApJ, 973, 53
Xuan, Z., Naoz, S., & Chen, X. 2023, PhRvD, 107, 043009
Xuan, Z., Naoz, S., Kocsis, B., & Michaely, E. 2024b, ApJ, 965, 148
Xuan, Z., Naoz, S., Kocsis, B., & Michaely, E. 2024a, PhRvD, 110, 023020
Xuan, Z., Naoz, S., Li, A. K. Y., et al. 2025, PhRvD, 111, 043018
Xuan, Z., Peng, P., & Chen, X. 2021, MNRAS, 502, 4199
Ye, C. S., Kremer, K., Chatterjee, S., Rodriguez, C. L., & Rasio, F. A. 2019, ApJ, 877, 122
Ye, C. S., Kremer, K., Ransom, S. M., & Rasio, F. A. 2024, ApJ, 975, 77
Ye, C. S., Kremer, K., Rodriguez, C. L., et al. 2022, ApJ, 931, 84
Zevin, M., Bavera, S. S., Berry, C. P. L., et al. 2021a, ApJ, 910, 152
Zevin, M., Pankow, C., Rodriguez, C. L., et al. 2017, ApJ, 846, 82
Zevin, M., Romero-Shaw, I. M., Kremer, K., Thrane, E., & Lasky, P. D. 2021b, ApJL, 921, L43
Zevin, M., Samsing, J., Rodriguez, C., Haster, C.-J., & Ramirez-Ruiz, E. 2019, ApJ, 871, 91
Zhang, F., Chen, X., Shao, L., & Inayoshi, K. 2021, ApJ, 923, 139
Zhang, Z., & Chen, X. 2024, ApJ, 968, 122
Zocchi, A., Gieles, M., Hénault-Brunet, V., et al. 2019, MNRAS, 482, 4713